



Partially oxidized ruthenium aerogel as highly active bifunctional electrocatalyst for overall water splitting in both alkaline and acidic media

Su Yan^{a,1}, Wenying Liao^{b,1}, Mengxiao Zhong^a, Weimo Li^a, Ce Wang^a, Nicola Pinna^c, Wei Chen^{b,d,*}, Xiaofeng Lu^{a,**}

^a Alan G. MacDiarmid Institute, College of Chemistry, Jilin University, Changchun 130012, China

^b Engineering Research Center of Industrial Biocatalysis, Fujian Province Higher Education Institutes, Fujian Provincial Key Laboratory of Advanced Materials Oriented Chemical Engineering, College of Chemistry and Materials Science, Fujian Normal University, Fuzhou 350007, China

^c Institut für Chemie, Humboldt-Universität zu Berlin, Brook-Taylor-Straße 2, 12489 Berlin, Germany

^d Fujian Provincial Key Laboratory of Theoretical and Computational Chemistry, Xiamen University, Xiamen 361005, China

ARTICLE INFO

Keywords:

Ruthenium
Aerogel
Partial oxidation
Electrocatalysis
Overall water splitting

ABSTRACT

In this study, a general strategy is demonstrated to prepare a partially oxidized three-dimensional (3D) porous ruthenium (Ru) aerogel with distinct porous architecture and unique Ru/RuO₂ interface. The optimized partially oxidized Ru aerogel catalyst exhibits an exceptional HER performance, which is even superior to the benchmark Pt/C catalyst, and an outstanding OER efficiency that is better than commercial RuO₂ in both alkaline and acidic solutions. Furthermore, a two-electrode configuration based on the partially oxidized Ru aerogel as both anode and cathode for the overall water splitting exhibits an ultra-low working voltage of 1.467 V in 1 M KOH and 1.468 V in 0.5 M H₂SO₄ at 10 mA cm⁻² as well as a satisfactory long-term stability, outperforming the device composed of Pt/C||RuO₂ catalysts. This research opens up a new avenue to develop highly efficient 3D porous aerogel electrocatalysts toward overall water splitting applications.

1. Introduction

The generation of hydrogen from electrocatalytic overall water splitting (EOWS) has attracted significant attention by the scientific community because of its potential to replace fossil fuels [1–6]. During the EOWS process, hydrogen evolution reaction (HER) and oxygen evolution reaction (OER) are the typical half reactions. Generally, high-efficiency electrocatalysts are usually required to reduce the overpotential and improve the reaction efficiency, such as Pt/C for HER and IrO₂ or RuO₂ for OER [7–9]. It is also worth noting that these outstanding electrocatalysts only perform well for HER or OER in different electrolytic electrolytes. Therefore, an inferior efficiency is usually achieved when assembling them to a cell for the EOWS in one medium (e.g. H₂SO₄ or KOH). To date, tremendous efforts have been committed to developing bifunctional electrocatalysts based on transition metal nanomaterials, however, the total efficiency and the stability of the EOWS on most of these catalysts need to be further improved

[10–17]. Especially, there is a serious lack of highly active bifunctional electrocatalysts toward EOWS in both alkaline and acidic solutions [18–21].

As an alternative to Pt, it has been demonstrated that metallic ruthenium (Ru) possesses a favorable hydrogen adsorption capability during HER process and also presents an evident economic advantage compared with Pt-based materials [22–24]. Furthermore, RuO₂ has been demonstrated to be one of the excellent OER electrocatalysts in an acidic electrolyte, but usually possess poor stability. In addition, although the OER performance of RuO₂ in an alkaline medium is good, it has been significantly fallen behind many previously reported OER catalysts. To improve the pH-universal HER performance of Ru-based materials, considerable effort has been devoted to alloy Ru with other transition metals and to support them onto various carbon materials. For example, CoRu alloy nanoparticles supported on carbon quantum dots (CoRu/CQDs) have been proposed as efficient catalysts for the HER. Due to the Ru-induced lattice strain and the optimized hydrogen bonding

* Corresponding author at: Engineering Research Center of Industrial Biocatalysis, Fujian Province Higher Education Institutes, Fujian Provincial Key Laboratory of Advanced Materials Oriented Chemical Engineering, College of Chemistry and Materials Science, Fujian Normal University, Fuzhou 350007, China.

** Corresponding author.

E-mail addresses: chenwei@fjnu.edu.cn (W. Chen), xflu@jlu.edu.cn (X. Lu).

¹ These authors contributed equally to this work.

energy, CoRu/CQDs catalyst presents an excellent HER performance in a broad pH range [25]. Our group recently demonstrated the fabrication of RuNi nanoparticles incorporated in N-doped carbon nanofibers (RuNi/NCNFs) as highly active bifunctional electrocatalysts toward both HER and OER, displaying an outstanding EOWS property in an alkaline electrolyte [26]. Recently, interface engineering via the integration of Ru with RuO₂ is considered as an efficient strategy to achieve highly electrocatalytic activity toward electrolytic water splitting because of the redistribution of charge density around the Ru/RuO₂ heterointerface that can reduce thermodynamic adsorption energy barriers of intermediates [27,28]. For example, core-shell Ru/RuO₂ nanorods fabricated by partial oxidation of Ru nanorods have been proposed as an electrocatalyst for EOWS and delivered overpotentials of 137 mV for HER and 320 mV for OER (@10 mA cm⁻²), respectively [29]. However, the electrocatalytic activity doesn't reach the required values, mostly owing to the low number of the active sites and the lack of continuous charge transfer channels. In another study, N-doped reduced graphene oxide decorated with Ru/RuO₂ nanoparticles (Ru/RuO₂@N-rGO) was prepared through a hydrothermal-calcining treatment, which could be used as high-efficiency HER and OER catalysts in alkaline and acidic solutions [30]. Benefiting from the 3D structure of rGO providing continuous charge transfer channels, the performance for EOWS has been significantly improved. However, considerable active metal components embedded into carbon material usually present reduced number of active sites, producing an unsatisfactory electrocatalytic performance. Additionally, these catalysts are generally prepared following complex synthesis routes and are subjected to post thermal annealing treatments under inert gas, which are not attractive for commercial applications.

Precious metal aerogels provide significant advantages in terms of excellent electrical conductivity, high porosity, large number of active sites for electrochemical applications [31–34]. For instance, a series of PdCu, PtCu and AuCu bimetallic aerogels have been prepared through a simple temperature-promoted reduction strategy for electrocatalytic ethanol oxidation. Resulting from the synergistic compositional and structural effects, the PdCu aerogel showed a much better ethanol oxidation activity than Pd aerogel and commercial Pd/C catalysts [35]. Recently, unsupported trimetallic PdAuPt aerogel has been reported to show an excellent performance toward the oxygen reduction reaction (ORR), also outperforming the state-of-the-art Pt/C catalysts [36]. Unfortunately, based on the yet limited number of examples of precious metal aerogels, their application in electrocatalysis is relatively limited and mostly concentrated on the alcohol oxidation reaction and ORR, although a few reports either on the HER or OER have been also published [37,38]. As far as we know, studies on the precious metal-based aerogels as bifunctional electrocatalysts toward the EOWS have not been reported so far.

Herein, we demonstrate a facile *in situ* reduction route to prepare a partially oxidized Ru aerogel as highly active electrocatalyst for the EOWS in both alkaline and acidic solutions. The Ru aerogel shows a porous architecture composed of interconnected nanoparticles, presenting a superior electron transport and abundant electrochemical active sites. Furthermore, the generation of RuO₂ from partial Ru oxidation modifies the electrochemical active sites and the adsorption energies of the reaction intermediates allowing to optimize the electrocatalytic activity. Our partially oxidized Ru aerogel displays exceptional HER and OER efficiencies in both alkaline and acidic solutions. A prototype cell for the EOWS, using Ru-30 aerogel as both anode and cathode, exhibits a working voltage of 1.467 V and 1.468 V (@10 mA cm⁻²) in alkaline and acidic solutions, respectively, which is significantly superior to a cell fabricated with benchmark Pt/C||RuO₂ catalysts. Furthermore, the EOWS device shows an excellent long-term stability.

2. Experimental section

2.1. Materials

RuCl₃·xH₂O and RuO₂ were commercially purchased from Sigma-Aldrich. NaBH₄ was provided by Sinopharm Chemical Reagent Co., Ltd. Commercial 20 wt% Pt/C was available by Johnson Matthey. All of the reagents were used without further purification.

2.2. Fabrication of partially oxidized Ru aerogel

First, Ru hydrogel was synthesized via a modified *in situ* spontaneous gelation process using one-step NaBH₄ reduction approach. Typically, freshly prepared NaBH₄ aqueous solution (5 mL, 0.3 M) was mixed with RuCl₃ solution (5 mL, 0.1 M). The molar ratio of the metal salt and reductant is 1:3. Quickly, the color of the reaction system becomes from black-brown to black. The bottle of the resulting solution was gently rotated for 1 min and kept at room temperature. After 5 h, the Ru hydrogel was obtained. Then, the as-prepared hydrogel was washed with deionized water for 5–6 times and then freeze-dried for 12 h to obtain the Ru aerogel. The partial oxidized Ru aerogel was obtained by controllable oxidation in air. Typically, the prepared Ru aerogel was put into muffle furnace under 350 °C for 30 min, named Ru-30 (Ru-60 was obtained by oxidizing at 350 °C for 60 min). Similarly, the Ru aerogels oxidized under 250 °C, 450 °C and 550 °C in muffle furnace for 30 min have also been prepared to be named as Ru-30 (250 °C), Ru-30 (450 °C), Ru-30 (550 °C).

2.3. Characterization

The morphology and chemical structure of the resultant products were studied using a field emission-scanning electron microscope (FE-SEM) (FEI Nova NanoSEM) and a transmission electron microscopy (TEM) (JEOL JEM-2000 EX) measurement. High-resolution TEM (HRTEM) images, energy dispersive X-ray (EDX) spectroscopy and mappings, selected area electron diffraction (SAED) patterns and scanning TEM (STEM) were performed using an FEI Tecnai G2 F20. X-ray diffraction (XRD) was carried out with PANalytical B.V. Empyrean measurement. X-ray photoelectron spectroscopy (XPS) was carried out with a Thermo Scientific ESCALAB250 system. Thermal Gravimetric Analyzer (TGA) was carried out with TGA2, Mettler Toledo. The aerogel density (ρ) value was calculated from the equation: $\rho = w/v$, where w is the weight of monolith aerogel, v is the spatial dimensions of aerogel.

2.4. Electrochemical measurements

Electrochemical tests were employed on a CHI660E electrochemistry workstation. The preparation of working electrode as follows: 2 mg of as-prepared catalyst and 10 μ L of Nafion 117 dispersion (5%) were added to 490 μ L ethanol, and vigorously sonicated for 1 h to form a homogeneous catalyst ink. After that, 50 μ L of the as-prepared catalyst ink was uniformly loaded on carbon paper surface (0.4 cm \times 0.49 cm, covered area: 0.196 cm²), and then dried under ambient condition. The catalyst ink of 20% Pt/C and RuO₂ were prepared with the same concentration for comparison. All catalysts for electrochemical tests with same loading density (1 mg cm⁻²). The standard Hg/HgO and Ag/AgCl electrodes were selected as the reference electrodes in 1 M KOH and 0.5 M H₂SO₄, respectively, and a Pt wire and a graphite rod were used as the counter electrode for OER and HER measurement, respectively. All the linear sweep voltammetry (LSV) measurements were conducted at a scan rate of 1 mV s⁻¹ with iR correction. Electrochemical impedance spectroscopy (EIS) was recorded with frequency range at 0.1–1000 kHz. For the electrochemical measurements in 1 M KOH, all potentials were converted to reversible hydrogen electrode (RHE) according to $E(\text{RHE}) = E(\text{Hg}/\text{HgO}) + 0.059 \times \text{pH} + 0.098$. In 0.5 M H₂SO₄, $E(\text{RHE}) = E(\text{Ag}/\text{AgCl}) + 0.059 \times \text{pH} + 0.197$. The EOWS measurement was carried in a

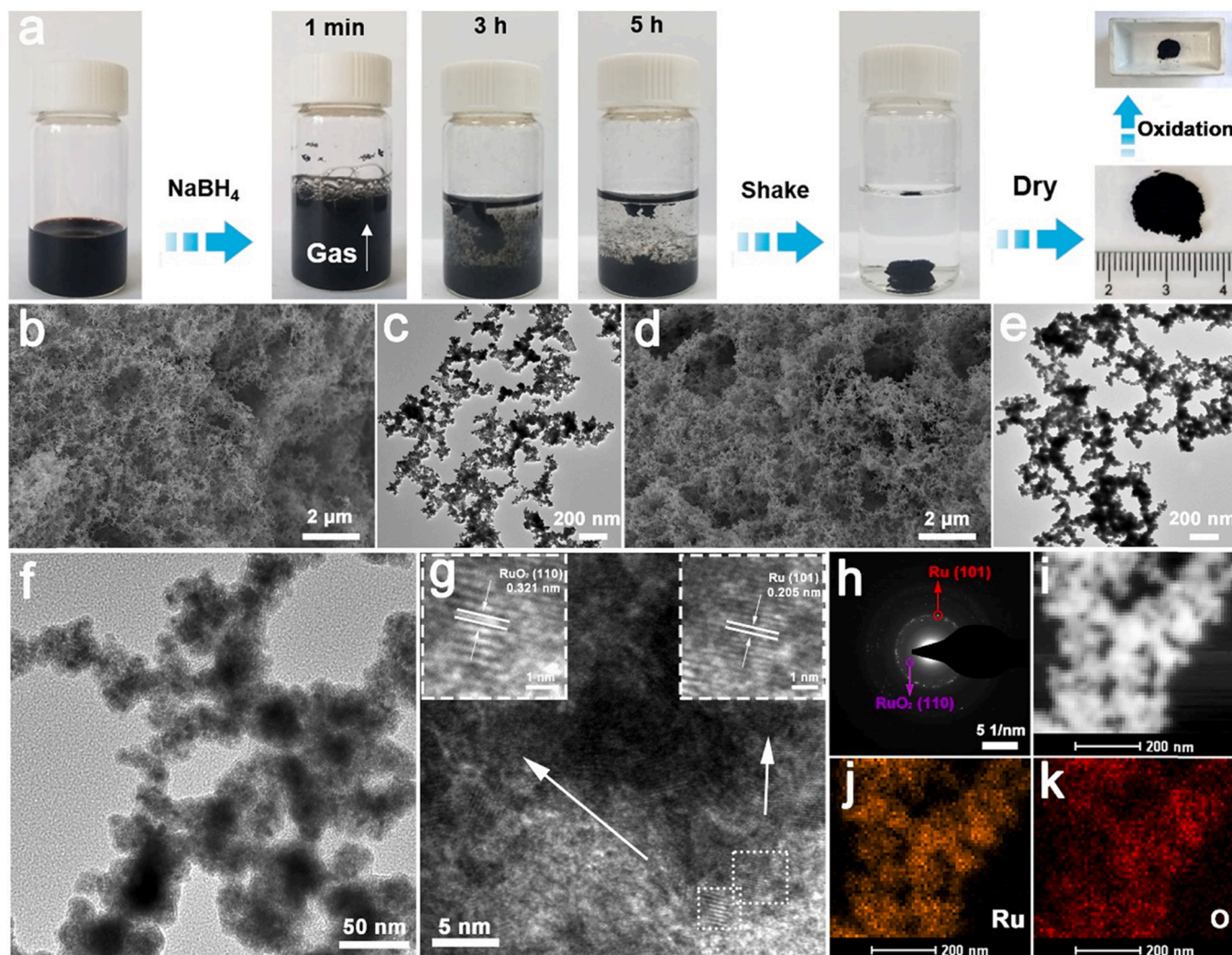


Fig. 1. (a) The synthetic procedure of partially oxidized Ru aerogel. FE-SEM images of the (b) Ru aerogel and (d) Ru-30 aerogel. TEM images of the (c) Ru aerogel and (e) Ru-30 aerogel. (f–k) TEM image in HRTEM mode, HRTEM image, SAED pattern, STEM micrograph and EDX mapping analysis of Ru and O elements of Ru-30 aerogel.

two-electrode system and the LSV curves for EOWS were obtained with a scan rate of 1 mV s^{-1} without iR-correction. The TOF value for HER was calculated from the equation: $\text{TOF} = (JA)/(2Fn)$, where J is the current density, A is the surface area of the working electrode, F is the Faraday constant (in C/mol), n is the moles of active sites.

3. Results and discussion

3.1. Synthetic process, morphological and structural characterization of partially oxidized Ru aerogel

As illustrated in Fig. 1a, Ru aerogel has been fabricated via an *in situ* spontaneous gelation process using NaBH₄ as a reducing agent. Briefly, due to its strong reducing ability when NaBH₄ is injected into a RuCl₃ aqueous solution, a black colloidal dispersion appears instantly, accompanied with substantial gas generation in the early stage. With prolonging time to approximately 5 h, a self-supported hydrogel is obtained. After a further purification and freeze drying process, the Ru aerogel is oxidized in air atmosphere at 350 °C for 30 min and 60 min to obtain partially oxidized Ru-30 and Ru-60, respectively. FE-SEM and TEM techniques are firstly used to characterize the morphology of the as-prepared Ru aerogel. As shown in Fig. 1b, the resultant Ru aerogel presents a 3D porous structure consisting of interconnected

nanoparticles that are fused randomly at various angles to form a network architecture. TEM image further demonstrates the formation of a bifurcated structure (Fig. 1c), which is similar with the morphologies of some precious metal aerogels reported in the previous literatures. [35, 37] According to the weight and volume of the partially oxidized Ru aerogel, the density is calculated to be 0.158 g cm^{-3} , which is in accordance with the previous report [39]. After oxidation, similar morphologies are also observed for Ru-30 (Fig. 1d,e) and Ru-60 (Fig. S1a,b), indicating that the whole morphology is well maintained and no significant change compared to that of Ru aerogel. In addition, since the calcination temperature is very important to achieve a high electrocatalytic activity, the morphologies of the partially oxidized Ru aerogel obtained under different heat treatment conditions are also investigated. As illustrated in Fig. S2, it is found that the size of the particles increases with the increasing of the temperature. Especially, the Ru-30(550 °C) sample presents a much large particle size and obvious agglomerates, which almost loses the porous advantage of the aerogel.

HRTEM is further conducted to reveal the chemical structure of the Ru-30. Lattice fringes corresponding to (101) plane of Ru at 0.205 nm and (110) plane of RuO₂ at 0.321 nm demonstrate the surface oxidation of Ru to RuO₂ after the annealing procedure (Fig. 1g,f). Moreover, metallic Ru lattice fringes are still present in the HRTEM image, proving

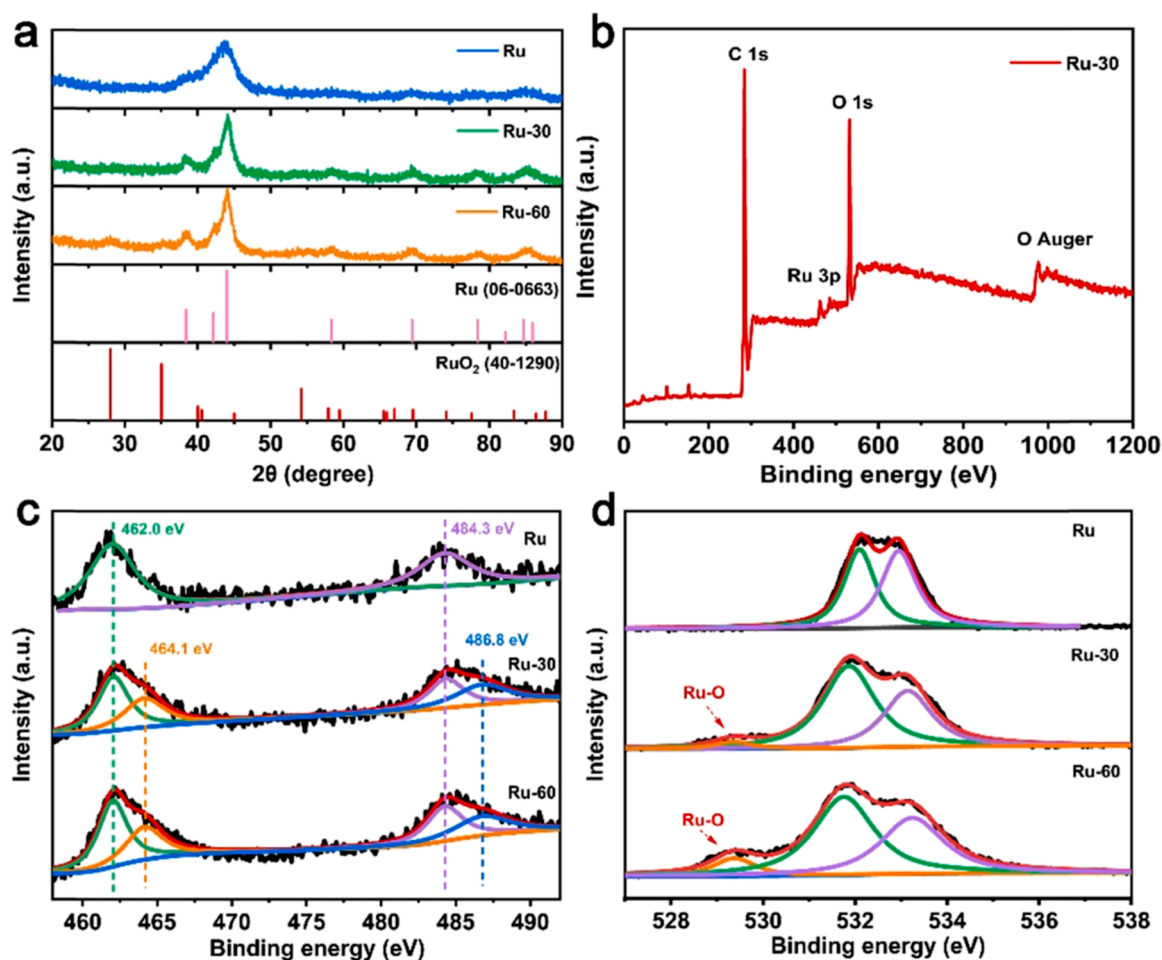


Fig. 2. (a) XRD patterns of Ru, Ru-30 and Ru-60 aerogel. (b–d) XPS survey, Ru 3p and O 1s spectra of Ru, Ru-30 and Ru-60 aerogel.

that Ru nanoparticles are not fully oxidized (Fig. S3). Fig. 1h displays the SAED pattern, and the (101) plane of Ru and (110) plane of RuO₂ are observed in the main Debye-Scherrer rings, further pointing to the partial oxidation of ruthenium in Ru-30 aerogel. The EDX spectrum exhibits strong Ru signal (Fig. S4), and the HAADF-STEM as well as corresponding EDX elemental mappings (Fig. 1i–k) distinctly reveal the homogeneous distribution of Ru and O. The crystallinity of all the samples is investigated by XRD, and the diffraction peaks of the Ru aerogel match well with the metallic Ru (JCPDS card No. 06-0663) (Fig. 2a). The most intense peak at $2\theta = 44^\circ$ corresponds to the diffraction of Ru (101) plane, which is consistent with the SAED pattern. Compared to the Ru aerogel, the partially oxidized Ru-30 and Ru-60 exhibit sharper reflections, demonstrating an enhanced crystallinity after oxidation. Moreover, it can be seen that the (110) reflection of RuO₂ (JCPDS card No. 40-1290) appears in Ru-60, confirming the formation RuO₂ from the oxidation of Ru, whereas there is no detectable signal of RuO₂ in Ru-30. Furthermore, TGA measurements of are performed to evaluate the weight percentage of the Ru and RuO₂ in the catalysts, which have been shown in Fig. S5. The result demonstrates that the Ru30 and Ru60 catalysts exhibit the similar weight percentage of Ru and RuO₂. Therefore, the difference of the RuO₂ reflection in the XRD patterns of the two catalysts of Ru-30 and Ru-60 is mainly due to their varied crystallinity. The catalyst with a low crystallinity is generally considered to be beneficial to enhance its electrocatalytic activity [40]. Additionally, from the XRD patterns of the samples synthesized under different heat treatment temperatures (Fig. S6), it is found that the intensity of the RuO₂ diffraction becomes significantly stronger with the increasing of the temperature, illustrating that more Ru components are

converted into RuO₂ under a high temperature.

XPS measurement is also employed to shed light on element compositions and oxidation states of the obtained samples. As displayed in Fig. 2b, the characteristic signatures of Ru and O elements can be clearly observed in the Ru-30 survey spectrum and similar results are also obtained for Ru aerogel and Ru-60 (cf. Fig. S7). The Ru 3p core spectra of the catalysts are displayed in Fig. 2c. A doublet is observed at 462.0 eV and 484.3 eV, which is associated with Ru⁰ 3p_{3/2} and Ru⁰ 3p_{1/2} states in Ru aerogel [41,42], and indicating that Ru³⁺ from RuCl₃ is reduced to Ru⁰ during the NaBH₄ reduction process. On the other hand, the peaks at 464.1 eV and 486.8 eV in Ru-30 are related to the Ru⁴⁺ 3p_{3/2} and Ru⁴⁺ 3p_{1/2}, further demonstrating the generation of RuO₂ in Ru-30. And Ru-60 presents similar features with Ru-30. The existence of RuO₂ in Ru-30 and Ru-60 is further confirmed from the analysis of the O 1s core spectrum. Specifically, the binding energy centered at 529.2 eV is assigned to oxygen in RuO₂, further confirming the existence of RuO₂ in both partially oxidized aerogels (Fig. 2d). The peaks located at 531.5 eV and 533.5 eV are attributed to the oxygen in OH⁻ surface species and of chemisorbed and physisorbed water on the surface.

3.2. Hydrogen evolution reaction

A standard three-electrode system is employed to estimate the HER activity of the obtained samples in different environments (alkaline medium: 1 M KOH, acidic medium: 0.5 M H₂SO₄). The HER activity of Ru aerogel oxidized with different time is firstly evaluated in 1 M KOH aqueous solution. As presented in Fig. 3a, the Ru-30 catalyst delivers the smallest overpotential of 36 mV (@ 10 mA cm⁻²) from LSV curves with

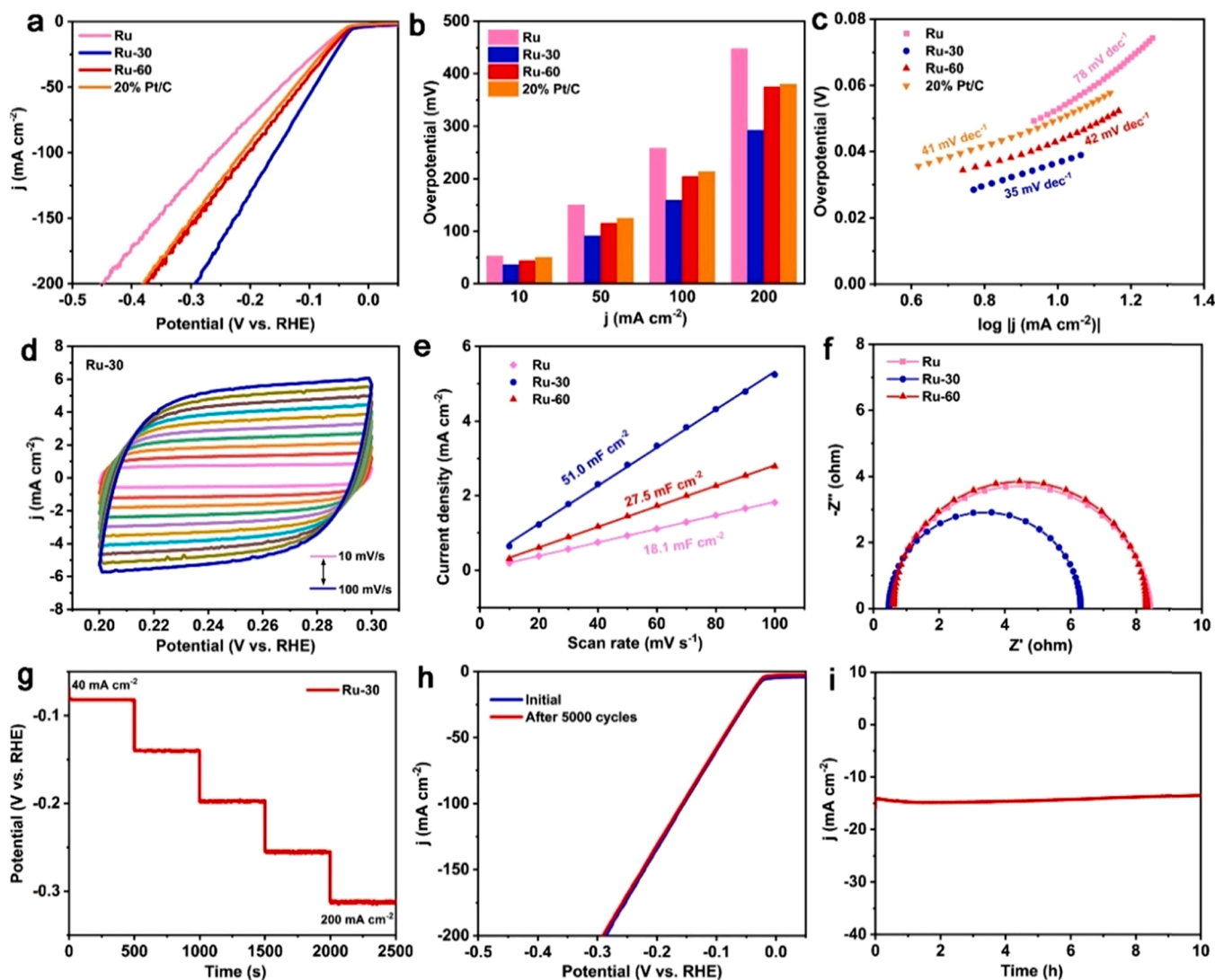


Fig. 3. HER performance (1 M KOH). (a) LSV curves for varied samples. (b) The overpotentials of different samples at 10, 50, 100 and 200 mA cm⁻². (c) Tafel plots of varied samples. (d) CV curves at different scan rates of Ru-30 (10–100 mV s⁻¹). (e) The C_{dl} calculated from capacitive current density ($\Delta j/2 = (j_a - j_c)/2$) vs scan rate of varied samples. (f) Nyquist plots for all the as-prepared samples. (g) Multi-current electrochemical process of Ru-30 catalyst. (h) LSV curves of Ru-30 catalyst before and after 5000 CV cycles. (i) The stability test for Ru-30 catalyst on a carbon paper.

iR correction, outperforming bare Ru (53 mV), Ru-60 (44 mV) and the benchmark 20% Pt/C catalyst (50 mV) as well as many precious metal-based catalysts for HER under an alkaline medium (Table S1). It is worth stressing that pristine Ru aerogel presents an outstanding HER efficiency close to Pt/C, which is attributed to the 3D porous structure of the aerogel providing a continuous conductive channel to realize faster electron transport and abundant active sites for H^{*} adsorption. Surprisingly, the Ru-30 aerogel catalyst exhibits a much better HER activity with the initial overpotential close to zero. Moreover, the overpotentials of Ru-30 at 50, 100 and 200 mA cm⁻² are only 91, 159 and 292 mV, respectively, considerably outperforming Pt/C and other control catalysts (Fig. 3b). The enhanced HER activity of the Ru-30 can originate from the heterostructure and the interface between Ru and RuO₂ components to induce electron transfer process from Ru to O atoms, endowing H^{*} with the appropriate adsorption state at the O site on the Ru-Ru bridge, which has been revealed of the density functional theory (DFT) in the following. Consequently, the thermodynamic energy barrier towards the HER decreases, resulting in a higher catalytic activity. Furthermore, Fig. S8a presents the HER activity of Ru aerogel samples that are calcined under different temperatures for 30 min. Clearly, Ru-30 (350 °C) catalyst exhibits the highest HER activity among all the as-

synthesized catalysts, especially at high current densities. To further explore the electrocatalytic reaction kinetics, Tafel plots transformed from LSV results are presented in Fig. 3c, Ru-30 displays the lowest Tafel slope value of 35 mV dec⁻¹ in 1 M KOH, better than that of Ru (78 mV dec⁻¹), Ru-60 (42 mV dec⁻¹) and the benchmark 20% Pt/C catalyst (41 mV dec⁻¹), implying that Ru-30 catalyst possesses a faster HER kinetics. Based on the Tafel slope range, the HER behavior of the Ru-30 catalyst follows the Volmer-Tafel mechanism in alkaline environment. The double-layer capacitance (C_{dl}) of Ru-30 is obtained from cyclic voltammetry (CV) under various scan rates (Fig. 3d), the CV curves for the other catalysts are shown in Fig. S9. The C_{dl} of 51.0 mF cm⁻² for Ru-30 is larger than that of Ru-60 (27.5 mF cm⁻²) and Ru aerogel (18.1 mF cm⁻²) (Fig. 3e), demonstrating that Ru-30 catalyst owns more electrochemical active centers. It is well known that the electrochemically active surface area (ECSA) of the as-synthesized samples is in direct proportion to the C_{dl} [43,44], which can be obtained from the equation: $ECSA = C_{dl}/C_s$ (C_s : the specific capacitance for a plane of 1 cm²) [45,46]. Therefore, the Ru-30 possesses the highest ECSA compared to the Ru aerogel and Ru-60. Furthermore, the TOF values of all the as-prepared samples are used to assess their intrinsic activity (Fig. S10). A higher TOF value of Ru-30 (0.031 s⁻¹) is achieved compared with that of Ru

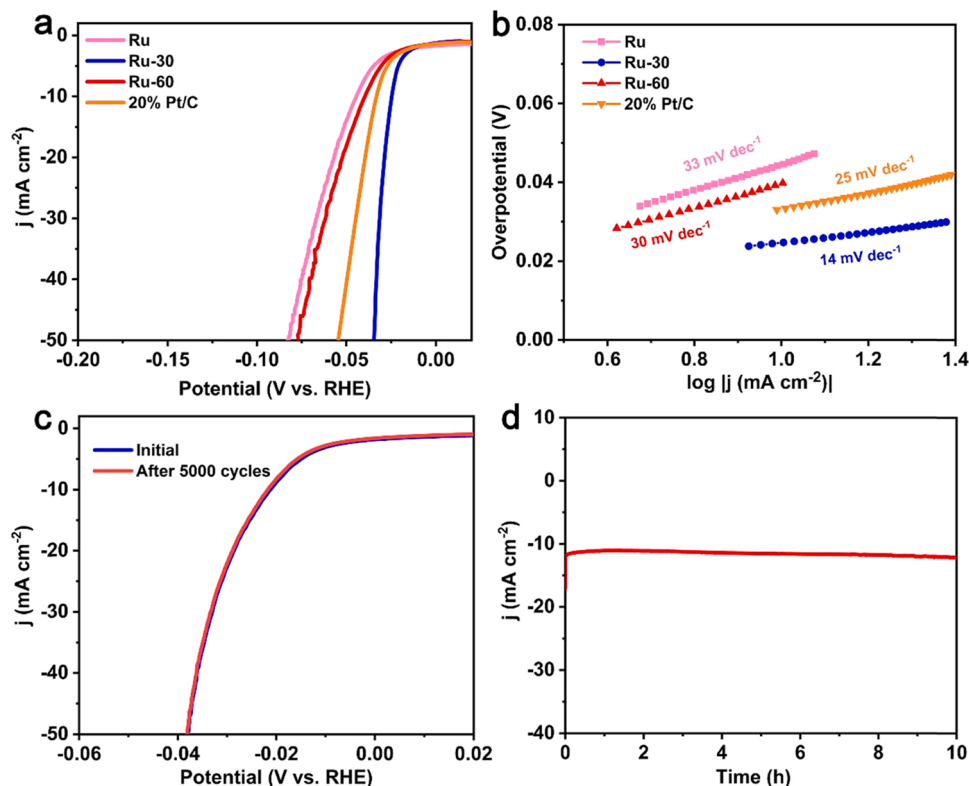


Fig. 4. HER performance (0.5 M H₂SO₄). (a) LSV curves for varied samples. (b) Corresponding Tafel plots of varied samples. (c) LSV curves of Ru-30 catalyst before and after 5000 CV cycles. (d) The stability test for Ru-30 on a carbon paper.

(0.015 s⁻¹) and Ru-60 (0.022 s⁻¹) at an overpotential of 100 mV, indicating the excellent activity of Ru-30 for HER in alkaline electrolyte. EIS measurement is used to evaluate the kinetics of a series of electrodes from the corresponding equivalent circuit model (Fig. S11). From

Fig. 3f, the Ru-30 electrode displays a lowest charge-transfer resistance (R_{ct}) of 6.11 Ω in comparison to Ru aerogel and Ru-60 electrodes, which facilitates charge transfer between catalyst and electrolyte, leading to a fast faradaic process and superior HER kinetics. In addition, multi-step

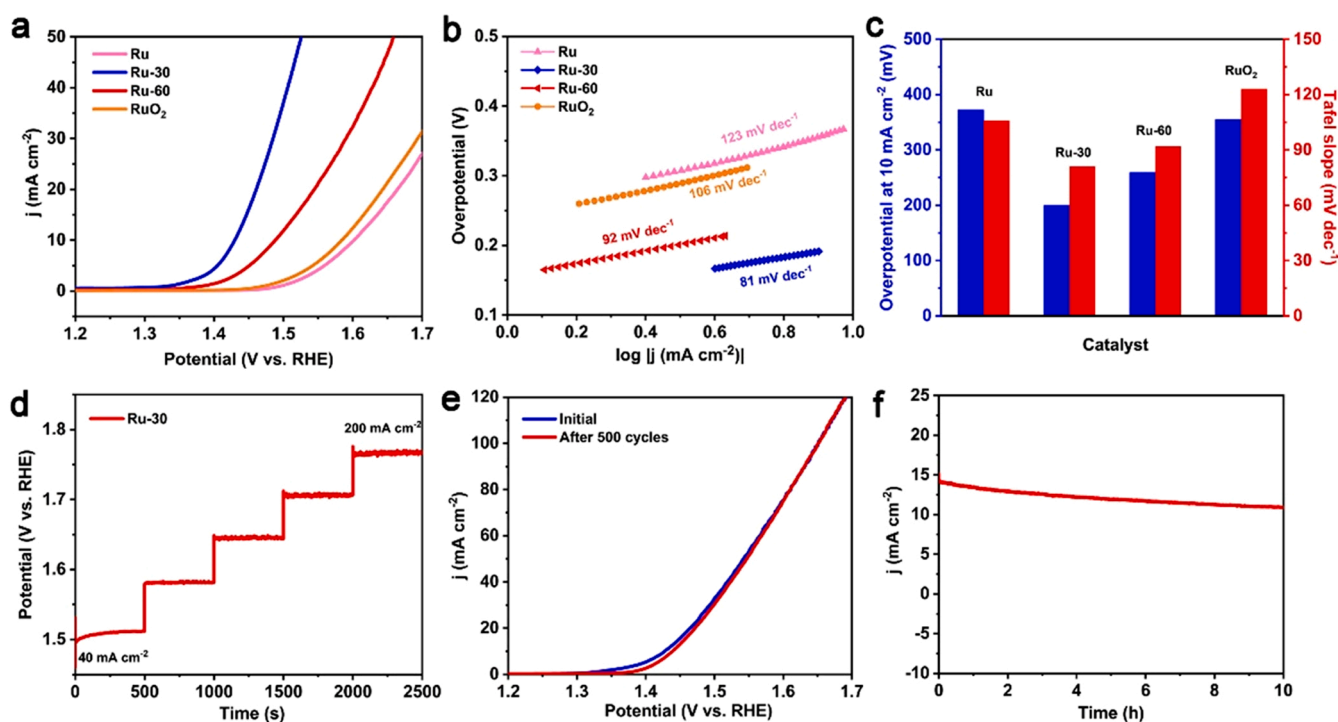


Fig. 5. OER performance (1 M KOH). (a) LSV curves for varied samples. (b) Tafel plots of varied samples. (c) The overpotential at 10 mA cm⁻² and Tafel slope of Ru-30. (d) Multi-current electrochemical process of Ru-30. (e) LSV curves of Ru-30 before and after 500 CV cycles. (f) The stability test for Ru-30 on a carbon paper.

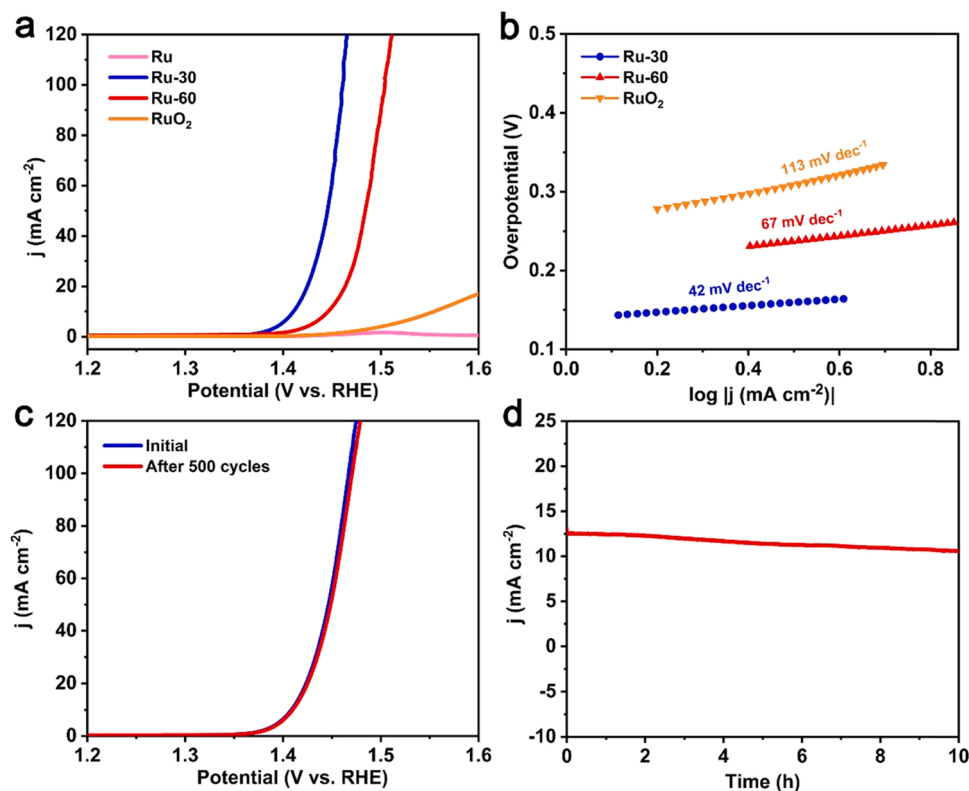


Fig. 6. OER performance (0.5 M H₂SO₄). (a) LSV curves for varied samples. (b) Tafel plots of varied samples. (c) LSV curves of Ru-30 catalyst before and after 500 CV cycles. (d) The stability test for Ru-30 catalyst on a carbon paper.

chronopotentiometric curves of Ru-30 at various current density (Fig. 3g) demonstrate a remarkable mass transport properties and mechanical robustness of the Ru-30 catalyst [47]. The durability of the Ru-30 is characterized by an accelerated degradation test. The LSV curves before and after 5000 CV cycles (Fig. 3h) present negligible changes, proving the excellent stability for HER in basic media. Chronoamperometric measurements for 10 h electrolysis further support this conclusion (Fig. 3i).

In addition to alkaline medium, the HER performance of the as-synthesized Ru-30 catalysts have also been studied in an acidic solution. As shown in the LSV curves (Fig. 4a), the overpotentials of Ru aerogel, Ru-30, Ru-60 and the benchmark Pt/C catalyst are 44, 24, 39 and 33 mV (@10 mA cm⁻²) with iR correction in 0.5 M H₂SO₄, respectively. It is remarkable that all the as-prepared Ru aerogel-based electrocatalysts exhibit outstanding HER efficiency even compared with some precious-metal-based catalysts in acidic conditions (Table S2). The HER activity of Ru aerogel samples that are calcined under different temperatures for 30 min has also been investigated. From the LSV curves (Fig. S8b), the activity of Ru-30 (350 °C) catalyst shows the smallest overpotential at a current density higher than 20 mA cm⁻² among all the catalysts. Furthermore, Ru-30 presents a lower Tafel slope (14 mV dec⁻¹) than Ru (33 mV dec⁻¹), Ru-60 (30 mV dec⁻¹) and 20% Pt/C (25 mV dec⁻¹), further implying that Ru-30 possesses a faster HER kinetics (Fig. 4b). Additionally, the Ru-30 aerogel catalyst also presents a good stability in an acidic medium with no significant changes in current density after 5000 CV cycles and 10 h chronoamperometric durability tests (Fig. 4c,d).

Overall, the excellent HER performance and stability of the as-prepared Ru-30 can be attributed to two main issues: 1) the inherent excellent conductivity and 3D porous structure of Ru-30 aerogel catalyst makes it very promising for highly efficient electron, ion and gas transport over the whole aerogel system and presents more exposed active sites to improve the reaction kinetics as well as exhibits excellent

mechanical properties for a favorable durability; 2) Benefitting from the optimized Ru/RuO₂ heterostructure, the Ru-30 aerogel has a favorable adsorption energy to improve the electron transfer and modulate the adsorption and desorption processes to promote the HER reaction kinetics.

3.3. Oxygen evolution reaction

The partially oxidized Ru aerogel also presents an outstanding OER electrocatalytic performance under both alkaline and acidic conditions. First, the OER activity of the Ru aerogel is investigated from polarization curves in 1 M KOH. In agreement to what has already been reported for metallic Ru, our as-synthesized Ru aerogel catalyst without oxidation also displays a similar poor OER activity, requiring an overpotential of 372 mV (@10 mA cm⁻²) (Fig. 5a). On the other hand, the OER activity of Ru-30 is significantly enhanced, and exhibits a low overpotential of 200 mV (@10 mA cm⁻²), outperforming many precious-metal-based OER catalysts in alkaline conditions (Table S3). With the increasing of the oxidation time, the overpotential also increases to 259 mV, which is much larger than that required by Ru-30. However, it is worth stressing that both of Ru-30/60 exhibit better OER activity than the benchmark RuO₂ (355 mV, 10 mA cm⁻²). The remarkable OER activity of Ru-30 may be resulting from the interfacial effect from the RuO₂ formed on the surface of the Ru nanoparticles, which can modulate the OER intermediates adsorption [48]. The influence of the calcination temperature of Ru-30 on the OER performances is also investigated. As shown in polarization curves (Fig. S8c), the Ru-30 (350 °C) catalyst exhibits the best OER activity. Besides, the superior OER performance of Ru-30 is also reflected on its Tafel plot (Fig. 5b,c), where Ru-30 exhibits the smallest Tafel slope (81 mV dec⁻¹) compared with Ru aerogel (123 mV dec⁻¹), Ru-60 (92 mV dec⁻¹) and RuO₂ (106 mV dec⁻¹), suggesting a fast OER kinetic. The multi-step chronopotentiometric curve demonstrates an excellent mass transport property of the Ru-30 catalyst

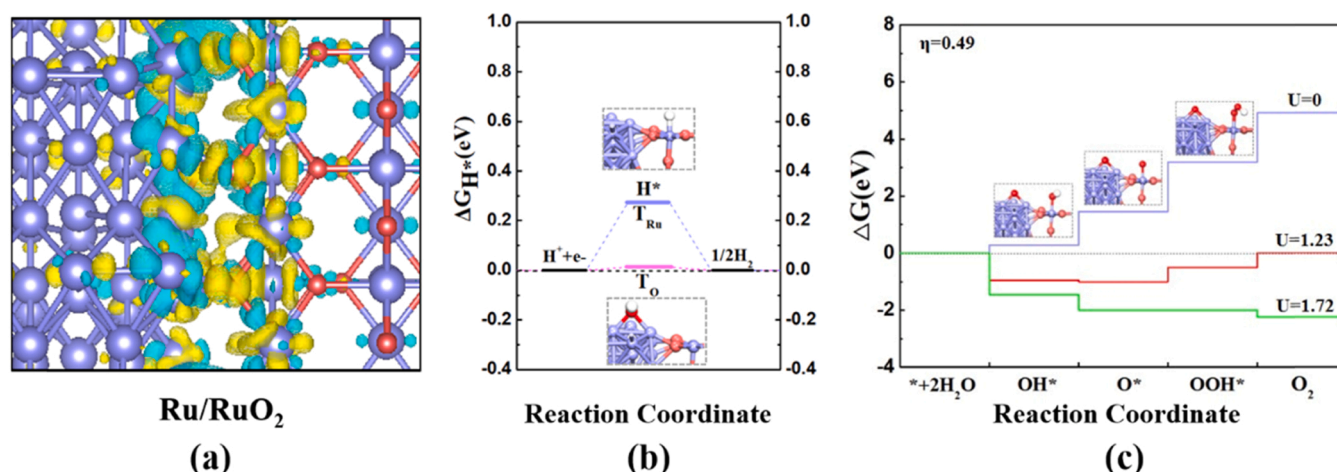


Fig. 7. (a) The charge density difference for the composite Ru/RuO₂ system, where the blue and yellow colors mean the decrease and increase of electron density, respectively. (b) The obtained ΔG_{H^*} of the adsorption sites on Ru/RuO₂. (c) The free-energy diagrams of OER on Ru/RuO₂ at the varied applied bias, in which the structures related to the adsorption of HO*, O*, and HOO* are provided. Here, the red, blue and white spheres correspond to O, Ru and H atoms, respectively.

during OER measurement in 1 M KOH (Fig. 5d). By comparing the LSV curves before and after 500 CV cycles, the overpotential at large current density presents almost no change (Fig. 5e), proving a satisfactory stability. Furthermore, the chronoamperometric response of the Ru-30 catalyst after a continuous OER test for 10 h at 1.53 V vs. RHE shows only a small decline of the current (Fig. 5f), further proving the excellent durability.

From the polarization curve (Fig. 6a), Ru-30 presents a lowest overpotential (181 mV) at 10 mA cm⁻² in 0.5 M H₂SO₄ compared with Ru-60 (217 mV) and RuO₂ (325 mV), respectively, also surpassing many precious-metal-based catalysts in acidic conditions (Table S4). Similar with that in 1 M KOH solution, the Ru-30 (350 °C) catalyst also shows the best OER activity in 0.5 M H₂SO₄ electrolyte (Fig. S8d). The outstanding OER performance of Ru-30 is further supported by its smallest Tafel slope (42 mV dec⁻¹) compared to Ru-60 (67 mV dec⁻¹) and RuO₂ (113 mV dec⁻¹) (Fig. 6b). Furthermore, Ru-30 aerogel displays a satisfactory stability by comparing the polarization curves before and after 500 CV cycles (Fig. 6c) and in 10 h of chronoamperometry measurements in 0.5 M H₂SO₄ (Fig. 6d).

3.4. DFT calculations for improved HER and OER mechanism

DFT calculation is a major means to investigate the mechanism of the electrocatalytic reaction [49,50]. To further understand the origin of HER activity of Ru/RuO₂ system, we carry out DFT calculations on it. As shown in Fig. S12, the theoretical slab model with the interface connecting the (101) facet of Ru and (110) facet of RuO₂ is used to simulate the Ru/RuO₂ composite structure. It is found that an obvious electron transfer takes place from Ru to RuO₂ parts (Fig. 7a). In view of the case that the water dissociation could bring some intermediates (e.g. OH, O, and H species), then we initially examine these species adsorption to acquire the stable surface phase by estimating the ΔG_{OH^*} , ΔG_{O^*} and ΔG_{H^*} values on the Ru/RuO₂ system (Table S5). It is found that the Ru-Ru bridge site at the interface has the strongest interaction with O*, reflected by the most negative ΔG_{O^*} value (Table S5). This result reveals that the O* prefers to occupy on the Ru-Ru bridge site at the interface. The detailed description is shown in the section 1.2 in the supporting information.

According to this structure, the HER activity of Ru/RuO₂ system is explored by calculating the ΔG_{H^*} values of possible catalytic sites (Fig. 7b). The results demonstrate a small ΔG_{H^*} value of only 0.011 eV at the O site, implying the superior HER activity (More details are shown in section 1.2 in supporting information). The probable mechanism for the superior HER activity is also analyzed in detail. It is found that the O

atom anchored on the Ru-Ru bridge site exhibits the *sp*³-hybridization, and two lone pairs are remained after forming two chemical bonds with two adjacent Ru atoms. Therefore, when H* attacks the O site, the valence electron of H and one lone pair of O atom can form one fully filled σ bonding orbital (σ_{O-H}) and one partially filled σ^* antibonding orbital (σ^*_{O-H}). Clearly, the occupation of electron in the σ^*_{O-H} orbital can determine the strength of O-H bond. In addition, in view of the great electronegativity of O atom, there is an electron transfer from Ru to O atoms (the calculated Bader charge is about -0.76 |e|), which can result in a more filled *p* states of O atom and an increasing of σ^*_{O-H} occupancy. As a result, when H* interacts with the O site, the bonding of O-H can be weakened, which endows H* with the appropriate adsorption state at the O site, contributing to the excellent HER activity.

The OER catalytic property is also investigated based on this structural model. As illustrated in Fig. 7c, under a bias of 0 V (blue lines), all steps can uniformly move uphill. When an equilibrium potential (*U* = 1.23 V) is applied, several steps can shift downhill while others stay uphill (red lines). Therefore, a potential should be applied so that every step moves downhill (green lines). The calculated results display that the required overpotential value can be as small as 0.49 V (Fig. 7c), suggesting a substantially high OER activity on the Ru/RuO₂ system, where the Ru atoms in the RuO₂ part at the interface act as the most active sites. Overall, the Ru/RuO₂ system presents superior catalytic properties toward HER and OER.

3.5. Characterization of the electrocatalysts after HER and OER processes

The Ru-30 aerogel catalyst is further characterized after HER and OER long-term stability tests in both alkaline and acidic solutions. First of all, the 3D porous structure is well maintained after HER process *cf.* SEM images in Fig. S13 and S14. Furthermore, the crystal structure was also well preserved as demonstrated by XRD measurements (Fig. S15 and S16), illustrating the excellent chemical and structural stability toward HER. Similarly, the SEM images in Fig. S17 and S18 prove that the porous 3D morphology and interconnected nanoparticle structure of Ru-30 is also well-preserved after the OER stability test in both alkaline and acidic solutions. However, after OER stability measurement, the intensities of the RuO₂ reflections at around $2\theta = 28^\circ$ and $2\theta = 35^\circ$ become more obvious in the XRD pattern (Fig. S19 and S20), suggesting that metallic Ru tends to be further oxidized during the OER electrocatalytic process [51,52]. Furthermore, the XPS measurement is performed on the catalysts after stability tests in both alkaline and acidic media to confirm the compositional stability (Fig. S21). The Ru 3p spectra of the post-HER and OER in 0.5 M H₂SO₄ share no evident changes with the fresh sample

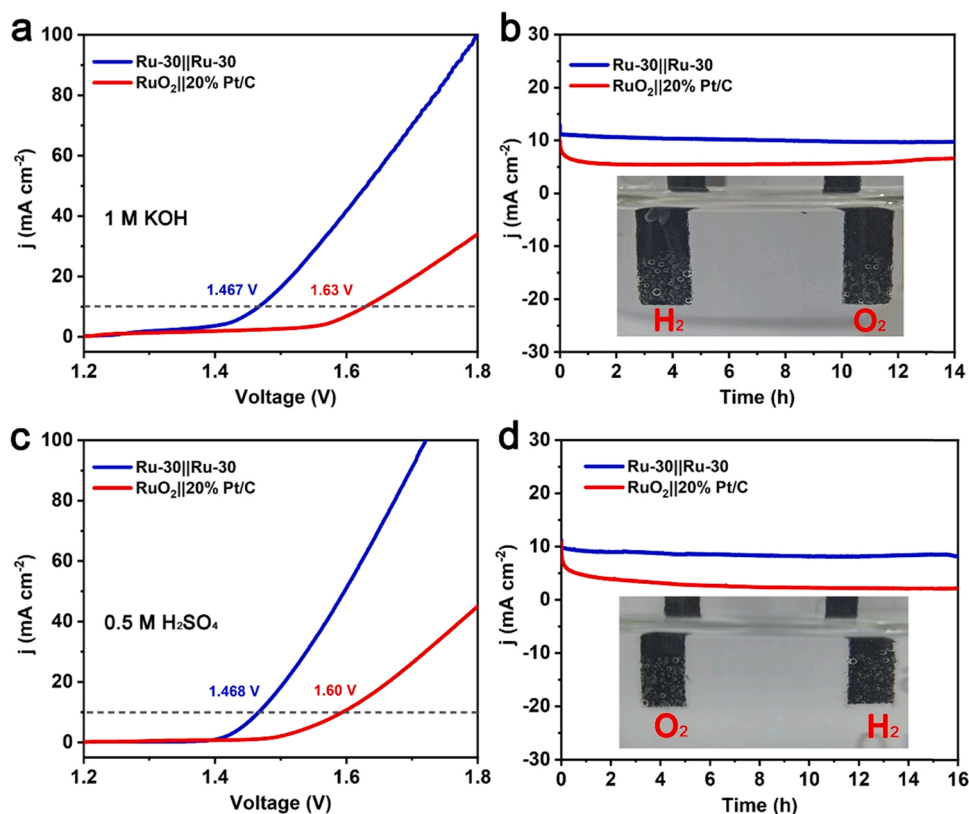


Fig. 8. LSV curves of EOWS devices based on Ru-30||Ru-30 and Pt/C||RuO₂ in a two-electrode configuration in (a) 1 M KOH and (c) 0.5 M H₂SO₄. The stability measurements of EOWS devices based on Ru-30||Ru-30 and Pt/C||RuO₂ in (b) 1 M KOH and (d) in 0.5 M H₂SO₄. The insets in (b) and (d) are the optical pictures of the electrodes in 1 M KOH and 0.5 M H₂SO₄.

and that in 1 M KOH display slightly positive shift. In addition, the signal intensity of RuO decreases obviously and Ru⁴⁺ increases significantly after OER stability test in 1 M KOH or 0.5 M H₂SO₄, indicating that metallic Ru tends to be converted to RuO₂ during the OER electrocatalytic process, which is consistent with the previous XRD results (Fig. S19 and S20). These results demonstrate that Ru-30 possesses a satisfactory HER and OER durability in both alkaline and acidic conditions.

3.6. Overall water splitting

Two-electrode electrolyzers employing Ru-30 catalyst supported on the carbon paper as both cathode and anode are constructed for the EOWS in 1 M KOH and 0.5 M H₂SO₄ (Supplementary Movie 1 and 2). From the LSV curve, it is estimated that only a working voltage of 1.467 V is achieved at 10 mA cm⁻² in 1 M KOH (Fig. 8a), much lower than those observed in commercial 20% Pt/C||RuO₂ (1.63 V) and many other electrolyzers consisting of precious metal-based electrocatalysts (Table S6). Furthermore, the durability of the Ru-30||Ru-30 electrolyzer is estimated by continuous operation at 1.48 V, showing only a little decrease in current after 14 h (Fig. 8b). Similarly, the EOWS in 0.5 M H₂SO₄ is also evaluated with a low working voltage of 1.468 V at 10 mA cm⁻² (Fig. 8c), outperforming many remarkable water splitting devices in acidic medium (Table S7). Chronoamperometric tests also demonstrate a better long-term stability under both alkaline and acidic conditions (Fig. 8d).

4. Conclusion

In summary, a partially oxidized Ru aerogel electrocatalyst is successfully synthesized and optimized to exhibit outstanding HER and OER performances in both alkaline and acidic conditions. The character

of porous structure, high electrical transport capability, and the interfacial effect between the RuO₂ and Ru components provides abundant electrochemical active sites, fast electron/mass transfer channels and efficient adsorption of the water splitting intermediates, resulting in an outstanding EOWS performance. Cell voltages below 1.5 V at 10 mA cm⁻² are obtained for the EOWS, which are superior to benchmark electrocatalysts combinations such as Pt/C||RuO₂. The partially oxidized Ru aerogel also presents satisfactory long-term stability in acidic and basic conditions. All in all, this study presents an easy and scalable way to prepare a new type of precious metal aerogel electrocatalysts with great potential to extend in practical applications in energy storage and conversion.

CRediT authorship contribution statement

Su Yan: Conceptualization, Methodology, Data curation, Writing – original draft. **Wenying Liao:** Methodology, Data curation. **Mengxiao Zhong:** Formal analysis. **Weimo Li:** Formal analysis. **Ce Wang:** Supervision, Visualization, Funding acquisition. **Nicola Pinna:** Supervision, Writing – review & editing. **Wei Chen:** Writing – review & editing, Supervision, Funding acquisition. **Xiaofeng Lu:** Writing – review & editing, Supervision, Funding acquisition.

Declaration of Competing Interest

The authors declare that they have no known competing financial interests or personal relationships that could have appeared to influence the work reported in this paper.

Acknowledgements

This work was financially supported by the National Natural Science

Foundation of China (51973079, 21875084, 21673093), the Project of the Education Department of Jilin Province, China (JJKH20211047KJ), the Natural Science Foundation of Fujian Province, China (2020J01147), Minjiang Scholar, Startup Fund for High-level Talent at Fujian Normal University, China and Program for Innovative Research Team in Science and Technology in Fujian Province University, China.

Appendix A. Supporting information

Supplementary data associated with this article can be found in the online version at doi:10.1016/j.apcatb.2022.121199.

References

- H.F. Wang, L. Chen, H. Pang, S. Kaskel, Q. Xu, MOF-derived electrocatalysts for oxygen reduction, oxygen evolution and hydrogen evolution reactions, *Chem. Soc. Rev.* 49 (2020) 1414–1448.
- I. Staffell, D. Scamman, A.V. Abad, P. Balcombe, P.E. Dodds, P. Ekins, N. Shah, K. R. Ward, The role of hydrogen and fuel cells in the global energy system, *Energy Environ. Sci.* 12 (2019) 463–491.
- J. Zhu, L. Hu, P. Zhao, L.Y.S. Lee, K.Y. Wong, Recent advances in electrocatalytic hydrogen evolution using nanoparticles, *Chem. Rev.* 120 (2020) 851–918.
- Z.W. Seh, J. Kibsgaard, C.F. Dickens, I. Chorkendorff, J.K. Nørskov, T.F. Jaramillo, Combining theory and experiment in electrocatalysis: Insights into materials design, *Science* 355 (2017) ead4998.
- I. Roger, M.A. Shipman, M.D. Symes, Earth-abundant catalysts for electrochemical and photoelectrochemical water splitting, *Nat. Rev. Chem.* 1 (2017) 0003.
- J. Wang, W. Cui, Q. Liu, Z. Xing, A.M. Asiri, X. Sun, Recent progress in cobalt-based heterogeneous catalysts for electrochemical water splitting, *Adv. Mater.* 28 (2016) 215–230.
- J.Y. Zhang, H. Wang, Y. Tian, Y. Yan, Q. Xue, T. He, H. Liu, C. Wang, Y. Chen, B. Y. Xia, Anodic hydrazine oxidation assists energy-efficient hydrogen evolution over a bifunctional cobalt perselenide nanosheet electrode, *Angew. Chem. Int. Ed.* 57 (2018) 7649–7653.
- T.N. Huan, G. Rousse, S. Zanna, I.T. Lucas, X. Xu, N. Menguy, V. Mougél, M. Fontecave, A dendritic nanostructured copper oxide electrocatalyst for the oxygen evolution reaction, *Angew. Chem. Int. Ed.* 56 (2017) 4792–4796.
- F. Gao, Y.P. Zhang, Z.Y. Wu, H.M. You, Y.K. Du, Universal strategies to multi-dimensional noble-metal-based catalysts for electrocatalysis, *Coord. Chem. Rev.* 436 (2021), 213825.
- Q. Hu, X.F. Liu, B. Zhu, L.D. Fan, X.Y. Chai, Q.L. Zhang, J.H. Liu, C.X. He, Z.Q. Lin, Crafting MoC₂-doped bimetallic alloy nanoparticles encapsulated within N-doped graphene as robust bifunctional electrocatalysts for overall water splitting, *Nano Energy* 50 (2018) 212–219.
- Y. Jia, L. Zhang, G. Gao, H. Chen, B. Wang, J. Zhou, M.T. Soo, M. Hong, X. Yan, G. Qian, J. Zou, A. Du, X. Yao, A heterostructure coupling of exfoliated Ni-Fe hydroxide nanosheet and defective graphene as a bifunctional electrocatalyst for overall water splitting, *Adv. Mater.* 29 (2017), 1700017.
- T. Ouyang, Y.Q. Ye, C.Y. Wu, K. Xiao, Z.Q. Liu, Heterostructures Composed of N-doped carbon nanotubes encapsulating cobalt and beta-Mo₂C nanoparticles as bifunctional electrodes for water splitting, *Angew. Chem. Int. Ed.* 58 (2019) 4923–4928.
- J. Jiang, P. Yan, Y. Zhou, Z. Cheng, X. Cui, Y. Ge, Q. Xu, Interplanar growth of 2D non-Van der Waals Co₂N-based heterostructures for efficient overall water splitting, *Adv. Energy Mater.* 10 (2020), 2002214.
- Y. Xu, W. Tu, B. Zhang, S. Yin, Y. Huang, M. Kraft, R. Xu, Nickel nanoparticles encapsulated in few-layer nitrogen-doped graphene derived from metal-organic frameworks as efficient bifunctional electrocatalysts for overall water splitting, *Adv. Mater.* 29 (2017), 1605957.
- X. Han, X. Wu, Y. Deng, J. Liu, J. Lu, C. Zhong, W. Hu, Ultrafine Pt nanoparticle-decorated Pyrite-type CoS₂ nanosheet arrays coated on carbon cloth as a bifunctional electrode for overall water splitting, *Adv. Energy Mater.* 8 (2018), 1800935.
- L.Q. Deng, K. Zhang, D. Shi, S.F. Liu, D.Q. Xu, Y.L. Shao, J.X. Shen, Y.Z. Wu, X. P. Hao, Rational design of Schottky heterojunction with modulating surface electron density for high-performance overall water splitting, *Appl. Catal. B-Environ.* 299 (2021), 120660.
- J.Q. Zhou, L. Yu, Q.C. Zhou, C.Q. Huang, Y.L. Zhang, B. Yu, Y. Yu, Ultrafast fabrication of porous transition metal foams for efficient electrocatalytic water splitting, *Appl. Catal. B-Environ.* 288 (2021), 120002.
- B. Zhang, F. Yang, X.D. Liu, N. Wu, S. Che, Y.F. Li, Phosphorus doped nickel-molybdenum aerogel for efficient overall water splitting, *Appl. Catal. B-Environ.* 298 (2021), 120494.
- S. Dutta, A. Indra, Y. Feng, H. Han, T. Song, Promoting electrocatalytic overall water splitting with nanohybrid of transition metal nitride-oxynitride, *Appl. Catal. B-Environ.* 241 (2019) 521–527.
- J. Mei, T. He, J. Bai, D. Qi, A. Du, T. Liao, G.A. Ayoko, Y. Yamauchi, L. Sun, Z. Sun, Surface-dependent intermediate adsorption modulation on iridium-modified black phosphorus electrocatalysts for efficient pH-universal water splitting, *Adv. Mater.* 33 (2021), 2104638.
- N.C.S. Selvam, L.J. Du, B.Y. Xia, P.J. Yoo, B. You, Reconstructed water oxidation electrocatalysts: the impact of surface dynamics on intrinsic activities, *Adv. Funct. Mater.* 31 (2021), 2008190.
- W. Li, Y. Liu, M. Wu, X. Feng, S.A.T. Redfern, Y. Shang, X. Yong, T. Feng, K. Wu, Z. Liu, B. Li, Z. Chen, J.S. Tse, S. Lu, B. Yang, Carbon-quantum-dots-loaded ruthenium nanoparticles as an efficient electrocatalyst for hydrogen production in alkaline media, *Adv. Mater.* 30 (2018), e1800676.
- Y. Zheng, Y. Jiao, Y. Zhu, L.H. Li, Y. Han, Y. Chen, M. Jaroniec, S.Z. Qiao, High electrocatalytic hydrogen evolution activity of an anomalous ruthenium catalyst, *J. Am. Chem. Soc.* 138 (2016) 16174–16181.
- J. Wang, Z.Z. Wei, S.J. Mao, H.R. Li, Y. Wang, Highly uniform Ru nanoparticles over N-doped carbon: pH and temperature-universal hydrogen release from water reduction, *Energy Environ. Sci.* 11 (2018) 800–806.
- W. Li, Y. Zhao, Y. Liu, M. Sun, G.I.N. Waterhouse, B. Huang, K. Zhang, T. Zhang, S. Lu, Exploiting Ru-induced lattice strain in CoRu nanoalloys for robust bifunctional hydrogen production, *Angew. Chem. Int. Ed.* 60 (2021) 3290–3298.
- M. Li, H. Wang, W. Zhu, W. Li, C. Wang, X. Lu, RuNi nanoparticles embedded in N-doped carbon nanofibers as a robust bifunctional catalyst for efficient overall water splitting, *Adv. Sci.* 7 (2020), 1901833.
- T. Qiu, Z. Liang, W. Guo, S. Gao, C. Qu, H. Tabassum, H. Zhang, B. Zhu, R. Zou, Y. Shao-Horn, Highly exposed ruthenium-based electrocatalysts from bimetallic metal-organic frameworks for overall water splitting, *Nano Energy* 58 (2019) 1–10.
- M. Zhang, J. Chen, H. Li, P. Cai, Y. Li, Z. Wen, Ru-RuO₂/CNT hybrids as high-activity pH-universal electrocatalysts for water splitting within 0.73 V in an asymmetric-electrolyte electrolyzer, *Nano Energy* 61 (2019) 576–583.
- R. Jiang, D.T. Tran, J. Li, D. Chu, Ru@RuO₂ core-shell nanorods: a highly active and stable bifunctional catalyst for oxygen evolution and hydrogen evolution reactions, *Energy Environ. Mater.* 2 (2019) 201–208.
- X. Gao, J. Chen, X. Sun, B. Wu, B. Li, Z. Ning, J. Li, N. Wang, Ru/RuO₂ nanoparticle composites with N-doped reduced graphene oxide as electrocatalysts for hydrogen and oxygen evolution, *ACS Appl. Nano Mater.* 3 (2020) 12269–12277.
- D. Wen, A.K. Herrmann, L. Borchardt, F. Simon, W. Liu, S. Kaskel, A. Eychmüller, Controlling the growth of palladium aerogels with high-performance toward bioelectrocatalytic oxidation of glucose, *J. Am. Chem. Soc.* 136 (2014) 2727–2730.
- R. Du, X. Jin, R. Hübner, X. Fan, Y. Hu, A. Eychmüller, Engineering self-supported noble metal foams toward electrocatalysis and beyond, *Adv. Energy Mater.* 10 (2019), 1901945.
- B. Cai, D. Wen, W. Liu, A.K. Herrmann, A. Benad, A. Eychmüller, Function-Led Design of Aerogels: Self-assembly of alloyed PdNi hollow nanospheres for efficient electrocatalysis, *Angew. Chem. Int. Ed.* 54 (2015) 13101–13105.
- J.M. Kim, J.H. Kim, J. Kim, Y. Lim, Y. Kim, A. Alam, J. Lee, H. Ju, H.C. Ham, J. Y. Kim, Synergetic structural transformation of Pt electrocatalyst into advanced 3D architectures for hydrogen fuel cells, *Adv. Mater.* 32 (2020), e2002210.
- C. Zhu, Q. Shi, S. Fu, J. Song, H. Xia, D. Du, Y. Lin, Efficient synthesis of MCu (M = Pd, Pt, and Au) aerogels with accelerated gelation kinetics and their high electrocatalytic activity, *Adv. Mater.* 28 (2016) 8779–8783.
- B. Cai, R. Hübner, K. Sasaki, Y. Zhang, D. Su, C. Ziegler, M.B. Vukmirovic, B. Rellinghaus, R.R. Adzic, A. Eychmüller, Core-shell structuring of pure metallic aerogels towards highly efficient platinum utilization for the oxygen reduction reaction, *Angew. Chem. Int. Ed.* 57 (2018) 2963–2966.
- R. Du, W. Jin, R. Hübner, L. Zhou, Y. Hu, A. Eychmüller, Engineering multimetallic aerogels for pH-universal HER and ORR electrocatalysis, *Adv. Energy Mater.* 10 (2020), 1903857.
- Q. Shi, C. Zhu, H. Zhong, D. Su, N. Li, M.H. Engelhard, H. Xia, Q. Zhang, S. Feng, S. P. Beckman, D. Du, Y. Lin, Nanovoid incorporated Ir_xCu metallic aerogels for oxygen evolution reaction catalysis, *ACS Energy Lett.* 3 (2018) 2038–2044.
- N. Hüsing, U. Schubert, Aerogels—airy materials: chemistry, structure, and properties, *Angew. Chem. Int. Ed.* 37 (1998) 22–45.
- S. Yan, M.X. Zhong, C. Wang, X.F. Lu, Amorphous aerogel of trimetallic FeCoNi alloy for highly efficient oxygen evolution, *Chem. Eng. J.* 430 (2022), 132955.
- J.S. Li, M.J. Huang, X.N. Chen, L.X. Kong, Y.W. Zhou, M.Y. Wang, J.L. Li, Z.X. Wu, X.F. Xu, Synergistically enhanced hydrogen evolution reaction by ruthenium nanoparticles dispersed on N-doped carbon hollow nanospheres, *Chem. Commun.* 56 (2020) 6802–6805.
- K. Tu, D. Tranca, F. Rodriguez-Hernandez, K. Jiang, S. Huang, Q. Zheng, M. X. Chen, C. Lu, Y. Su, Z. Chen, H. Mao, C. Yang, J. Jiang, H.W. Liang, X. Zhuang, A novel heterostructure based on RuMo nanoalloys and N-doped carbon as an efficient electrocatalyst for the hydrogen evolution reaction, *Adv. Mater.* 32 (2020), 2005433.
- C.C. McCrory, S. Jung, J.C. Peters, T.F. Jaramillo, Benchmarking heterogeneous electrocatalysts for the oxygen evolution reaction, *J. Am. Chem. Soc.* 135 (2013) 16977–16987.
- Y. Liu, X. Liang, L. Gu, Y. Zhang, G.D. Li, X. Zou, J.S. Chen, Corrosion engineering towards efficient oxygen evolution electrodes with stable catalytic activity for over 6000 h, *Nat. Commun.* 9 (2018) 2609.
- Y. Fu, H.-Y. Yu, C. Jiang, T.-H. Zhang, R. Zhan, X. Li, J.-F. Li, J.-H. Tian, R. Yang, NiCo alloy nanoparticles decorated on N-doped carbon nanofibers as highly active and durable oxygen electrocatalyst, *Adv. Funct. Mater.* 28 (2018), 1705094.
- Y.J. Li, H.C. Zhang, T.H. Xu, Z.Y. Lu, X.C. Wu, P.B. Wan, X.M. Sun, L. Jiang, Underwater superhydrophobic pine-shaped Pt nanorod array electrode for ultrahigh-performance hydrogen evolution, *Adv. Funct. Mater.* 25 (2015) 1737–1744.
- Y. Hou, M. Qiu, M.G. Kim, P. Liu, G. Nam, T. Zhang, X. Zhuang, B. Yang, J. Cho, M. Chen, C. Yuan, L. Lei, X. Feng, Atomically dispersed nickel-nitrogen-sulfur species anchored on porous carbon nanosheets for efficient water oxidation, *Nat. Commun.* 10 (2019) 1392.

- [48] J. Kim, P.C. Shih, K.C. Tsao, Y.T. Pan, X. Yin, C.J. Sun, H. Yang, High-performance pyrochlore-type yttrium ruthenate electrocatalyst for oxygen evolution reaction in acidic media, *J. Am. Chem. Soc.* 139 (2017) 12076–12083.
- [49] J.J. Ding, D.C. Wu, J.H. Zhu, S.H. Huang, F. Rodríguez-Hernández, Y. Chen, C. B. Lu, S.Q. Zhou, J.C. Zhang, D. Tranca, X.D. Zhuang, High-entropy carbons: from high-entropy aromatic species to single-atom catalysts for electrocatalysis, *Chem. Eng. J.* 426 (2021), 131320.
- [50] C. Lu, K. Jiang, D. Tranca, N. Wang, H. Zhu, F. Rodríguez-Hernández, Z. Chen, C. Yang, F. Zhang, Y. Su, C. Ke, J. Zhang, Y. Han, X. Zhuang, Electrochemical reduction of carbon dioxide with nearly 100% carbon monoxide faradaic efficiency from vacancy-stabilized single-atom active sites, *J. Mater. Chem. A* 9 (2021) 24955–24962.
- [51] J. Yang, Q. Shao, B. Huang, M. Sun, X. Huang, pH-universal water splitting catalyst: Ru-Ni nanosheet assemblies, *iScience* 11 (2019) 492–504.
- [52] N. Cao, K. Hu, W. Luo, G.Z. Cheng, RuCu nanoparticles supported on graphene: a highly efficient catalyst for hydrolysis of ammonia borane, *J. Alloy. Compd.* 590 (2014) 241–246.